We are IntechOpen, the world's leading publisher of Open Access books Built by scientists, for scientists

4,800
Open access books available

122,000
International authors and editors

135M
Downloads

Our authors are among the

154
Countries delivered to

TOP 1%
most cited scientists

12.2%
Contributors from top 500 universities

WEB OF SCIENCE™

Selection of our books indexed in the Book Citation Index in Web of Science™ Core Collection (BKCI)

Interested in publishing with us?
Contact book.department@intechopen.com

Numbers displayed above are based on latest data collected.
For more information visit www.intechopen.com

20

Self-Assembly of Nanoparticles at Solid and Liquid Surfaces

Peter Siffalovic, Eva Majkova, Matej Jergel,
Karol Vegso, Martin Weis and Stefan Luby
Institute of Physics, Slovak Academy of Sciences
Slovakia

1. Introduction

The research field of nanoparticle synthesis and related nanoparticle applied sciences have been steadily growing in the past two decades. The chemical synthesis of nanoparticles was improved up to the point that the organic and inorganic nanoparticle colloids are produced with a low size dispersion and with a well defined nanoparticle shape in large quantities. A stunning feature of a drying nanoparticle colloidal solution is the ability to create self-assembled arrays of nanoparticles. The self-assembled nanoparticle arrays mimic the natural crystals. The size of perfectly ordered domains is limited by the size dispersion of nanoparticles. Consequently the defects in the self-assembled structure are obvious and unavoidable. Despite these defects, the self-assembled nanoparticle arrays represent a new class of nanostructures built on "bottom-up" technological approach to fabrication. The traditional way of "top-down" fabrication technology primarily based on nano-lithography is complex, including many technological steps, time consuming and expensive. The main advantage is the tight control of all parameters governing the final nanostructures. On the other hand, the emerging fabrication technologies based on the self-assembled nanoparticles are fast, less complex and more price competitive. An extensive research is now focused on a deeper understanding of processes that control the self-assembly. New routes for directed or stimulated self-assembly are studied to achieve a tighter control than readily available in the spontaneous self-assembly. In this chapter we will discuss the spontaneous nanoparticle self-assembly with emphasis on characterization of nanoparticle arrays at various stages of the self-assembly process. The main diagnostic technique used throughout this chapter will be the grazing-incidence small-angle X-ray scattering (GISAXS) that represents a reliable and simple monitor of nanoparticle arrangement. The theoretical background of GISAXS and required instrumentation are described in Section 2. The most flexible surface to study the nanoparticle self-assembly processes is the liquid surface. The Section 3. reviews the latest results of studies combing the GISAXS technique with Langmuir nanoparticle layers on the water subphase. Almost all relevant nanoparticle applications rely on self-assembled arrays on solid surfaces. The Section 4 describes in detail the possibilities of nanoparticle transfer from liquid onto solid surfaces. The post-processing of self-assembled nanoparticle arrays and their applications are reviewed in the last Section 5.

2. SAXS/GISAXS techniques and their employment for nanoparticle research

The transmission (TEM) and scanning (SEM) electron microscopy provide information on the nanoparticle shape, average size and size distribution. However, this information is usually obtained after numerical evaluation of real space micrographs from limited data sets. Alternative approach is based on the angle-resolved analysis of scattered X-rays or neutrons from the nanoparticles and their assemblies. In this chapter we will employ the small-angle X-ray scattering (SAXS) (Guinier and Fournet 1955) for the nanoparticle colloidal solutions. For nanoparticles immobilized at interfaces, a related technique so-called grazing-incidence small-angle X-ray scattering (GISAXS) is used that has been recently reviewed (Renaud, Lazzari et al. 2009). A general scheme of the GISAXS experiment is shown in Fig. 1.

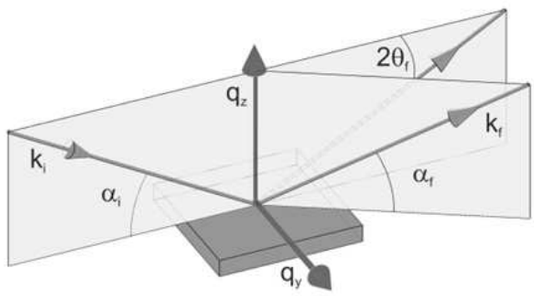

Fig. 1. The GISAXS measurement geometry

The collimated X-ray beam defined by $\vec{k}_i$ is incident under a small grazing angle on the sample surface. The scattered radiation is recorded by a two dimensional X-ray detector. Each point at the detector plane receives the scattered radiation given by a set of two angles ($2\theta_f$, α_f) that corresponds to a unique scattering vector $\vec{q}$ in the reciprocal space. The relationship between the scattering vector in reciprocal space and the scattering angles in the real space is given by the following equations (Müller-Buschbaum 2009)

$$\begin{aligned} q_x &= \frac{2\pi}{\lambda}\left[cos(2\theta_f)cos(\alpha_f) - cos(\alpha_i)\right] \\ q_y &= \frac{2\pi}{\lambda}\left[sin(2\theta_f)cos(\alpha_f)\right] \\ q_z &= \frac{2\pi}{\lambda}\left[sin(\alpha_f) + sin(\alpha_i)\right] \end{aligned} \tag{1}$$

The SAXS/GISAXS signal is given by constructive interferences of X-ray waves partially scattered on individual nanoparticles. The total scattered intensity (also called the scattering cross-section) at specific $\vec{q}$ vector in the reciprocal space is given as (Feigin, Svergun et al. 1987)

$$I(\vec{q}) = \sum_{i=1}^{N}\sum_{j=1}^{N} F^i(\vec{q}).F^{j,*}(\vec{q}).exp\left[i\vec{q}.(\vec{r}_i - \vec{r}_j)\right] \tag{2}$$

where N is the total number of nanoparticles, $F^i(\vec{q})$ is the form-factor of the i^{th} nanoparticle and $\vec{r}_i$ defines the position of the i^{th} nanoparticle. Within the simple Born (kinematic) approximation (BA) the nanoparticle form-factor is simply given by the Fourier transform of the nanoparticle density function $\rho_i(\vec{r})$ as follows (Glatter and Kratky 1982)

$$F^i(\vec{q}) = \int \rho_i(\vec{r}).exp(i\vec{q}.\vec{r})d\vec{r} \tag{3}$$

For the nanoparticles immobilized at interfaces we have to include the refraction/reflection phenomena at the interfaces and the associated multiple scattering events. This is treated in detail within the framework of the distorted-wave Born approximation (DWBA) which introduces a modified form-factor for each nanoparticle confined near the interface (Holý, Pietsch et al. 1999). A detailed survey of the DWBA theory can be found in the following reference (Renaud, Lazzari et al. 2009). A typical DWBA effect is the presence of the Yoneda enhancement at the critical exit angle in the GISAXS patterns (Yoneda 1963). In many cases we can avoid the DWBA multiple scattering terms by recording the GISAXS pattern at the incident angle several times larger than the critical angle for the total X-ray reflection of the supporting substrate (Daillant and Gibaud 2009). If we assume that the nanoparticles can be described by an average form-factor $\left\langle |F(\vec{q})|^2 \right\rangle$ than the eq. (2) in BA can be rearranged as follows

$$I(\vec{q}) = N \left\langle |F(\vec{q})|^2 \right\rangle S(\vec{q}) \tag{4}$$

Here the $S(\vec{q})$ represent the nanoparticle interference function. The nanoparticle interference function is the reciprocal space equivalent of the nanoparticle pair correlation function $P(\vec{r})$ defined in real space (Lazzari 2009). The pair correlation function is proportional to the probability of finding a nanoparticle at the position vector $\vec{r}$ centered at an arbitrarily selected nanoparticle. This function is directly accessible from the TEM/SEM micrographs.

The GISAXS experimental technique was confined for a long time to synchrotron facilities as the scattering cross-section is generally very low. Each synchrotron ring has a dedicated SAXS beamline that can support conventional GISAXS setup. The Fig. 2 shows the typical GISAXS scheme of the BW4 beamline at the DORIS III ring at HASYLAB, Hamburg (Stribeck 2007). The front-end of the experimental setup is a wiggler that generates the X-ray radiation. The crystal monochromator is used to select a single wavelength typically at 0.139 nm. The radiation is further conditioned with slits and two cylindrical mirrors to focus the radiation in both directions at the detector plane. The additional beryllium X-ray lenses can be attached to focus the radiation at the sample position (Roth, Dohrmann et al. 2006).

The distance between the sample and detector can vary between 3 m and 13 m that allows flexibility in the accessible range of the reciprocal space. The two-dimensional (2D) X-ray CCD detector is used to record the X-ray radiation scattered by the sample. The primary and specularly reflected beams are suppressed by the beamstops.

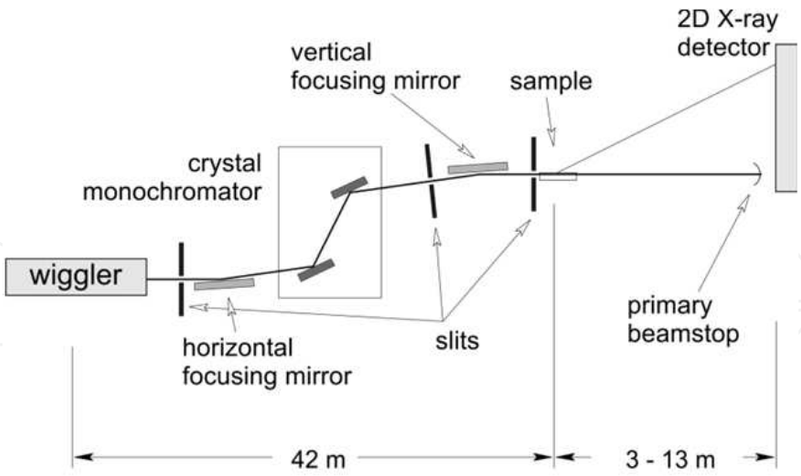

Fig. 2. The sketch of the experimental GISAXS geometry at BW4 beamline, HASYLAB

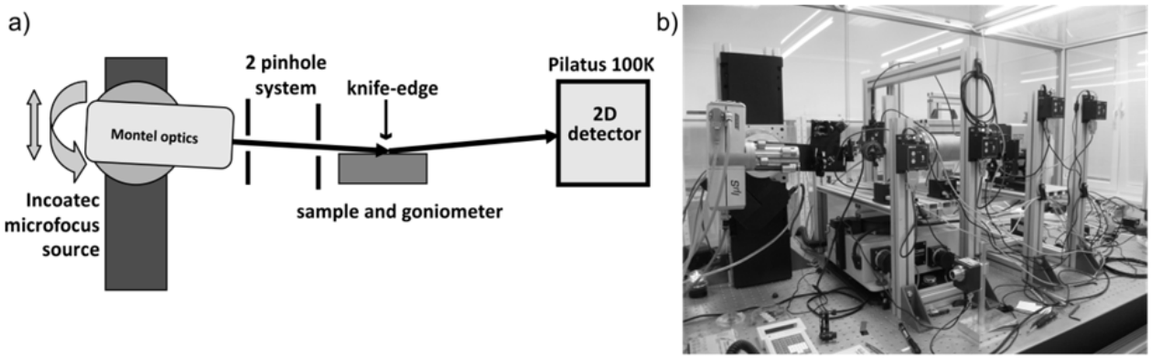

Fig. 3. a) The scheme of the laboratory GISAXS setup and (b) the photograph of its realization at Institute of Physics SAS.

The latest advances in the low-power X-ray generators and the efficient X-ray optics opened a new era of laboratory equipments suitable for GISAXS measurements (Michaelsen, Wiesmann et al. 2002). Nowadays already several companies (Bruker AXS, Anton Paar, Hecus XRS, Rigaku) supply complete X-ray solutions supporting GISAXS measurement modes for solid-state samples. The Fig. 3a and Fig. 3b show the laboratory setup scheme and the photograph of a home-built GISAXS instrumentation developed at the Institute of Physics SAS, respectively (Siffalovic, Vegso et al. 2010). This setup supports GISAXS measurements on solid as well as liquid surfaces. The core of the experimental apparatus is a compact low-power (30 W) X-ray source (Cu-K_α) equipped with a loosely focusing X-ray Montel optics (Wiesmann, Graf et al. 2009). The source can be freely rotated and translated in the vertical direction. This is important for the precise adjustment of the incident angle in the GISAXS measurements at liquid surfaces. The unwanted scattered radiation is eliminated by laser-beam precisely cut tungsten pinholes. The sample is fixed on a goniometer that allows precise height and tilt adjustments.

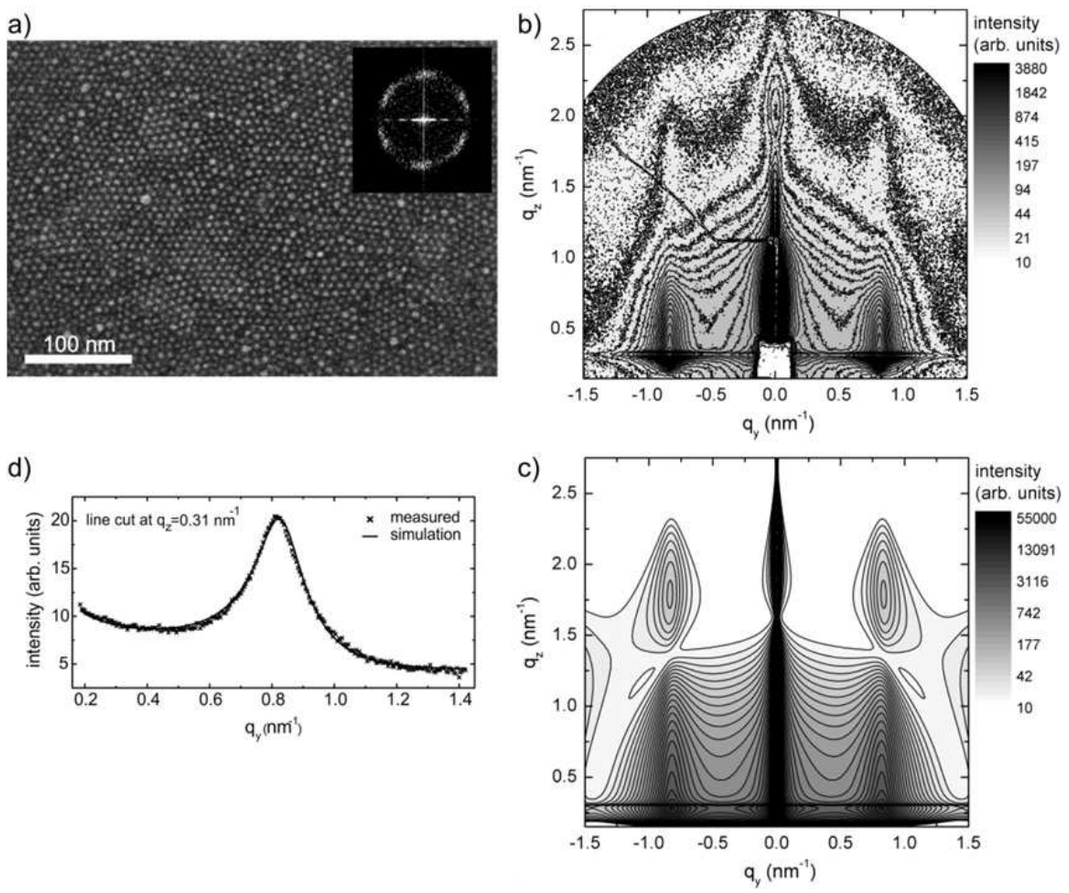

Fig. 4. a) The SEM micrograph of Fe-O self-assembled nanoparticles. Measured (b) and simulated (c) GISAXS pattern of self-assembled nanoparticles. d) The extracted line-cut from the measured GISAXS pattern along with the simulation.

The auxiliary knife-edge blade is used to reduce the parasitic air-scattering. The additional vacuum flight-tube can be inserted between the sample and the X-ray detector to reduce the air scattering and absorption. The detector used is a fast acquisition CMOS based 2D X-ray detector of PILATUS detector family (Kraft, Bergamaschi et al. 2009).

To illustrate the capability of the GISAXS technique to characterize the self-assembled nanoparticle monolayers we use an example of iron oxide nanoparticles (Siffalovic, Majkova et al. 2007). The Fig. 4a shows the SEM image of a self-assembled array of iron oxide nanoparticles. The inset of Fig. 4a shows the Fourier transform of SEM micrograph with partially smeared-out spots corresponding to the hexagonal arrangement. The smearing-out is due to mutually misaligned nanoparticle domains originating from finite nanoparticle size dispersion which is in sharp contrast to natural atomic crystals. The Fig. 4a and 4b show the measured and simulated GISAXS pattern, respectively. The characteristic side maxima located at the $q_{iy} \approx \pm 0.82 nm^{-1}$ are the "finger prints" of the self-assembly in the nanoparticle array. In the first approximation, the mean interparticle separation can be estimated from

the side maximum position in the reciprocal space as $\Delta \approx 2\pi/q_y \approx 7.7nm$. This simple estimation is valid only for a slowly varying nanoparticle form-factors within the kinematic BA. A precise fitting of the measured GISAXS data using the full DWBA theory can provide further information on the nanoparticle size and size dispersion as well as their correlation length (Lazzari 2002). The Fig. 4d shows a line cut extracted from the measured GISAXS pattern with the corresponding fit. The fitted nanoparticle diameter was 6.1±0.6 nm and the lateral correlation length in the nanoparticle array was 87 nm. It has to be noted that colloidal nanoparticles are covered by a surfactant shell to avoid their spontaneous agglomeration in colloidal suspensions. In the case of Fe-O nanoparticles discussed above, oleic acid and oleylamine were used. A GISAXS pattern fitting provides basic information on the metallic-like nanoparticle core size while the organic shell is rather invisible for X-rays. On the other hand, the positions of the side maxima in the GISAXS pattern are always connected with the interparticle distance which is affected by the surfactant shell. This example clearly demonstrates the ability of GISAXS technique to extract main nanoparticle parameters in the self-assembled arrays. The main advantage is that the GISAXS technique does not require any specific sample environment conditions such as vacuum nor special sample preparation. On the other hand it can be applied even in very aggressive environments such as UV/ozone reactor (Siffalovic, Chitu et al. 2010). Moreover, a rapid GISAXS data acquisition in millisecond range can be used for a real-time in-situ probing of nanoparticle reactions and self-assembly processes (Siffalovic, Majkova et al. 2008).

3. Nanoparticle self-assembly at liquid/air interfaces

In the last ten years we have seen a tremendous progress in the colloidal nanoparticle chemistry (Feldheim 2002; Nagarajan 2008; Niederberger and Pinna 2009). The refined chemical synthesis routes can produce large quantities of highly monodisperse nanoparticles in colloidal solutions with the size dispersion below 10 % (Park, An et al. 2004). The low nanoparticle dispersion is the "holy grail" of the large-scale nanoparticle self-assembly (Pileni 2005). Being able to prepare nanoparticles with zero size dispersion, we could fabricate genuine artificial nanoparticle crystals competing with natural ones in terms of the structure perfection and long-range order. However the finite nanoparticle size dispersion permits only a limited extent of ordering in nanoparticle self-assembled arrays. A typical model for description of the real nanoparticle assemblies is the paracrystal model (Hosemann and Bagchi 1962; Guinier 1963). Here a paracrystal order parameter summed up with the mean interparticle distance defines degree of the array perfection.

The colloidal nanoparticle solutions can be applied on a solid substrate directly or in two steps, utilizing liquid surface for self-assembly with a subsequent transfer onto a solid substrate. Drop casting followed by solvent evaporation is an example of the former method (Chushkin, Ulmeanu et al. 2003) that proved to be successful e.g. for preparation of large-area self-assembled arrays of noble metal nanoparticles with the diameter of a few tens nm. In addition to the nanoparticle size, surfactant type affects the self-assembly as well. For smaller nanoparticles, such as those presented in this chapter with the diameter below 10 nm, a direct application of the colloidal nanoparticle solutions on solid substrate produces only locally well assembled regions but is not suitable for large-area nanoparticle depositions. Here, the latter above mentioned method is promising as it will be shown later. The GISAXS technique can be employed to track the nanoparticle assemblies in rapidly

drying colloidal solution at solid surfaces (Siffalovic, Majkova et al. 2007). We used the focused X-ray beam to map the nanoparticle self-assembly at arbitrary selected position within the colloidal drop. The Fig. 5 shows the three typical GISAXS patterns.

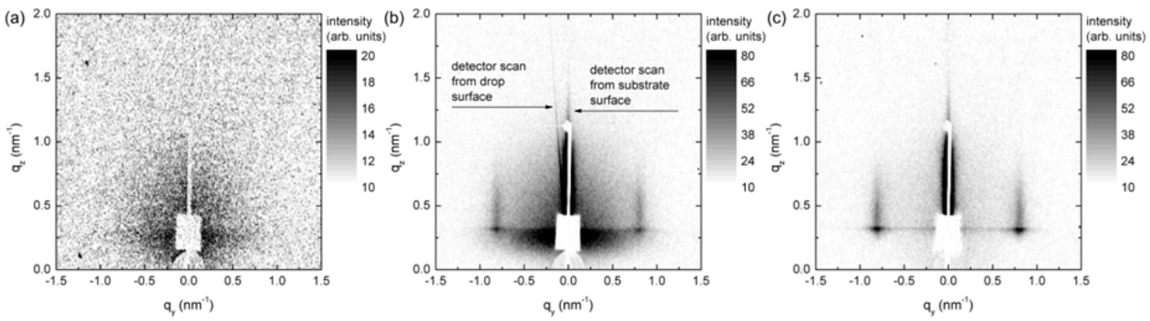

Fig. 5. The GISAXS pattern recorded from a drying colloidal Fe-O nanoparticle drop at three different stages: a) directly after drop casting, b) intermediate phase. c) dried colloidal drop.

The Fig. 5a shows the GISAXS pattern directly after application of a colloidal Fe-O nanoparticle solution onto silicon substrate. The GISAXS pattern does not show any maxima typical for self-assembled nanoparticle layers. The visible scattering in the GISAXS pattern is characteristic for a diluted nanoparticle solution and can be described by the nanoparticle form-factor. The Fig. 5b shows the intermediate state when the X-ray beam partially passes through the colloidal drop surface. The scattering streaks originating from interfaces also called "detector scans" are visible. The first one can be attributed to the scattering from the substrate surface and the second one originates from the colloidal drop surface. The angle between the two detector streaks directly maps the angle between the normal of substrate surface and the normal of the probed colloidal drop surface. The side maxima belong to the already dried self-assembled areas. The Fig. 5c shows the final GISAXS pattern after the colloidal solution is completely evaporated. The interparticle distance of final nanoparticle assembly are clearly manifested in the GISAXS pattern by the side maxima.

The spatially static GISAXS technique can track the nanoparticle assembly only in one selected probing volume within the evaporating colloidal drop. In order to monitor various probe volumes inside the colloidal nanoparticle drop during the self-assembly process we introduced a scanning GISAXS technique. The scanning GISAXS method is based on the fast vertical or horizontal scanning of the evaporating colloidal drop by the probing X-ray beam (Siffalovic, Majkova et al. 2008). The sketch of the scanning GISAXS technique is shown in Fig. 6a. The colloidal drop composed of iron oxide nanoparticles dispersed in toluene was applied onto silicon substrate located on a vertically scanning goniometer. As the evaporating drop was gradually scanned across the incoming X-ray beam we continuously recorded X-ray scattering from three different drop zones. In the zone Z0 the X-ray beam passed above the evaporating drop. These data were used for the background correction. In the zone Z1 we recorded exclusively the X-ray scattering originating from the drying drop surface and drop interior. In the zone Z2 we additionally detected the X-ray scattering coming from the substrate surface. The Fig. 6b shows the line cuts extracted from the GISAXS frames taken in zone Z1 corresponding to the three different stages of the colloidal drop evaporation process: 1.) directly after drop casting, 2.) intermediate state, and 3.) final state characterized by the complete solvent evaporation. It is important to notice that the

experimental data for all three evaporation stages can be fitted solely using the nanoparticle form-factor function. According to the eq. (4) the interference function is constant in this case, i.e. $S(\vec{q}) = 1$.

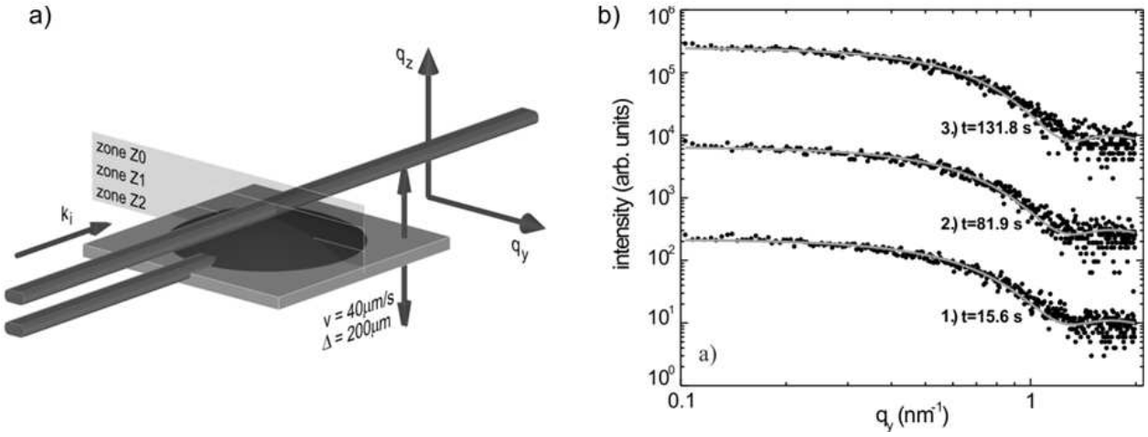

Fig. 6. a) The scheme of the GISAXS scanning technique. b) The GISAXS pattern line cuts at the critical exit angle for the three different stages of the colloidal Fe-O nanoparticle drop evaporation.

This means that the nanoparticles do not create self-assembled domains at the evaporating drop surface or in its volume at any time that suggests the origin of the nanoparticle self-assembly to be located at the three-phase boundary as predicted for a drying drop of dispersed particles (Deegan, Bakajin et al. 1997). The scanning GISAXS technique clearly demonstrates the ability to track the nanoparticle self-assembly process in real-time with millisecond time resolution.

As mentioned above, colloidal nanoparticles are usually terminated by surfactant molecules to avoid spontaneous agglomeration in colloidal suspensions. The nanoparticles with hydrophobic termination allow self-assembly at liquid/air interfaces and formation of Langmuir films in the form of simple 2D systems (Ulman 1991). Controlling the surface pressure by changing the nanoparticle layer area and the temperature of the subphase, we can produce large-area and homogenous self-assembled nanoparticle layers. The electron microscopy techniques including SEM, TEM or scanning probe techniques (AFM, STM) cannot be utilized to monitor the nanoparticle self-assembly at liquid/air interface. The visible/UV optical microscopy and Brewster angle microscopy are limited in resolution due to diffraction limit (Born and Wolf 1999). For a certain kind of metal and metal oxide nanoparticles exhibiting plasmonic properties (Au, Ag, Al, Cu) the interparticle distance can be indirectly monitored by the energy shift in localized surface plasmon resonance due to the dipole-dipole coupling of excited plasmons in the self-assembled nanoparticle arrays (Rycenga, Cobley et al. 2011). On the other hand the GISAXS technique can be employed to directly monitor the interparticle distance in self-assembled arrays directly in the Langmuir trough. The laboratory GISAXS setup shown in Fig. 3 was used to record the GISAXS patterns of Ag nanoparticles (6.2±0.7 nm) directly in the Langmuir trough. The GISAXS patterns of self-assembled Ag nanoparticles with oleic acid as surfactant at the surface pressures of 16 mN/m and 26 mN/m are shown in Fig. 7a and Fig. 7b, respectively.

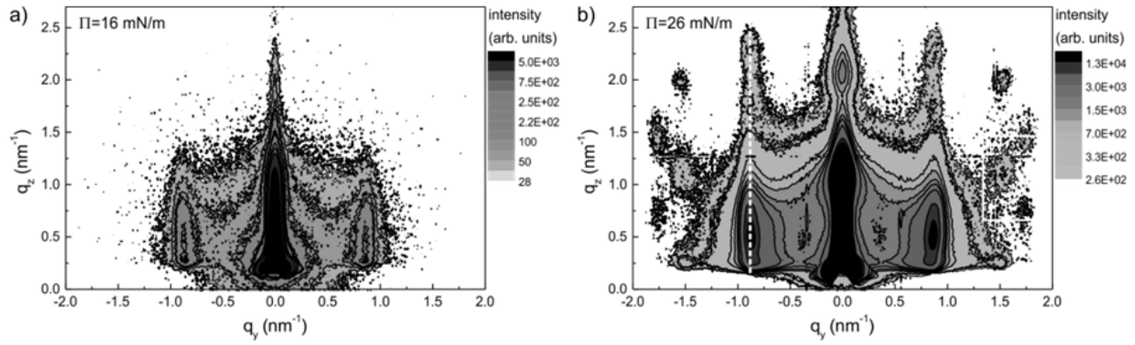

Fig. 7. The GISAXS patterns of self-assembled Ag nanoparticle Lagmuir films at surface pressure a) 16 mN/m and b) 26 mN/m.

The surface pressure of 16 mN/m corresponds to a closed nanoparticle monolayer on the water surface. The interference function produces two symmetrical side maxima at $q_y \approx \pm 0.87 nm^{-1}$ (truncation rods) corresponding to the average interparticle distance of 7.2 nm. The higher order side maxima are absent due to the short exposition time. The two-dimensional nanoparticle monolayer has a constant interference function in the q_z direction where the modulation visible on the truncation rods is produced solely by the nanoparticle form-factor (Holý, Pietsch et al. 1999). At the surface pressure of 26 mN/m, the second nanoparticle layer forms and changes the observed GISAXS pattern (Vegso, Siffalovic et al. 2011). The newly formed nanoparticle vertical correlation perpendicular to the Langmuir film plane results in the modulation of the observed truncation rod depicted by the dashed white line in Fig. 7b. It can be shown that the modulation along the truncation rod is associated with the second nanoparticle layer laterally shifted in analogy with the "AB stacking" in solid state crystals (Kittel 2005). The presence of the second layer can be verified also by distinct second order maxima in Fig. 7b. The presented GISAXS results show the possibility to study not only the lateral but also the vertical nanoparticle correlations in 3D nanoparticle assemblies that is due to the ability of GISAXS to inspect non-destructively buried layers and interfaces. This useful feature of the GISAXS technique to study the buried vertical correlations of interfaces was already applied in studies of multilayered thin films (Salditt, Metzger et al. 1994; Siffalovic, Jergel et al. 2011).

Recently we have performed in-situ real-time studies of compression and decompression of Ag nanoparticle Langmuir films. We were interested in the correlation between the macroscopic elastic properties of nanoparticle layers and microscopic layer parameters like the interparticle distance. As a convenient measure of macroscopic elastic properties we use the surface elastic modulus defined as (Barnes, Gentle et al. 2005)

$$E = -A\left(\frac{\partial \Pi}{\partial A}\right)_T \tag{1}$$

Here Π is the measured surface pressure of the nanoparticle layer with the area A at a constant subphase temperature T. The Fig. 8 shows the evaluated side maximum position along the q_y direction in the GISAXS reciprocal space map similar to the one shown in Fig. 7a.

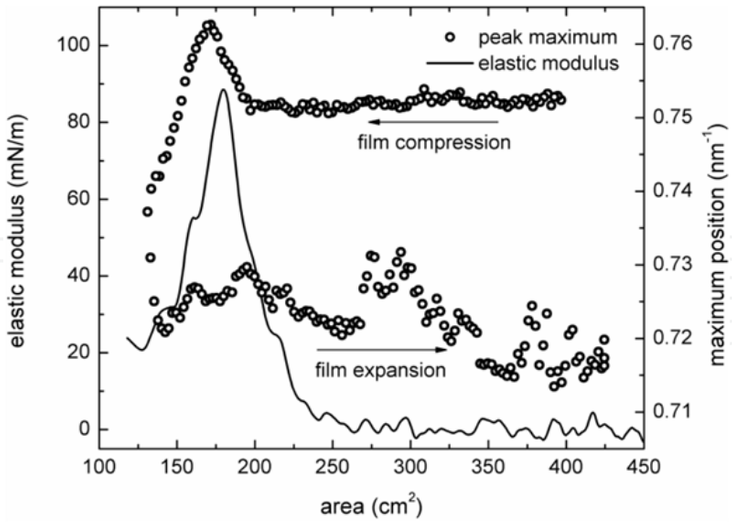

Fig. 8. The evaluated GISAXS peak maximum position and the surface elastic modulus of the Ag nanoparticle layer at water/air interface as a function of the layer area.

After spreading the nanoparticle solution onto the water subphase, the nanoparticles assemble into small clusters with hexagonal ordering that has been identified by independent ex situ experiments (to be published). Increasing the surface pressure by reducing the layer area results in the formation of a continuous monolayer without a change of the interparticle distance. This compression stage is characterized by a constant elastic modulus as the isolated nanoparticle clusters are joining into larger entities. At surface area of approximately 250 cm² we observe an increase in the elastic modulus peaking at the area of 180 cm². This stage can be associated with the densification of the nanoparticle layer accompanied by the nanoparticle rearrangements along the individual cluster boundaries and cluster coalescence. At the maximum of surface elastic modulus we observe also a slight compaction of the nanoparticle layer at nanoscale indicated by the change of the interparticle distance. This phase ends up with a compact nanoparticle layer. A further compression of the nanoparticle layer results in the formation of a second nanoparticle layer that induces a sudden drop in the elastic modulus and significant release of the mean interparticle distance. The nanoparticles forming the second layer create vacancies in the first one that is accompanied by deterioration of the order in the first nanoparticle layer. In this case the paracrystal model of the nanoparticle layer predicts a shift of the maximum to lower q_y values in the reciprocal space (Lazzari 2009) that was confirmed by this experimental observation. After the decompression the interparticle distance in the nanoparticle layer does not relax to the initial value. It has to be noted that the second layer formation and tendency to form 3D ordered nanoparticle assemblies was demonstrated here for Ag nanoparticles with oleic acid as surfactant, however, other types of metallic nanoparticles with other type of surfactant may behave differently. This example shows the benefit of GISAXS technique to precisely monitor microscopic parameters of the nanoparticle assemblies prior to the deposition onto solid substrates that will be discussed in the following section.

4. Transfer of self-assembled layers from liquid onto solid surfaces

In the previous section we discussed the formation of nanoparticle monolayers at water/air interface. The Langmuir film represented by self-assembled nanoparticle monolayer seems to be the most promising candidate for the homogenous deposition of large-area nanoparticle arrays. The two important questions are remaining. The first one is: "What is the suitable surface pressure for deposition and how to monitor it?" The second one is: "How to transfer the Langmuir film onto solid substrate with a minimum damage of the self-assembled layer?" In this section we try to give answers to them.

The first question was partially addressed in the previous section. We have shown the GISAXS technique gives a precise tool to monitor the monolayer formation at nanoscale. In Fig. 8 we showed the evolution of the interparticle distance with increasing surface pressure and we related formation of the second nanoparticle layer to a sudden drop in the observed surface elastic modulus. Additionally, we can track the evolution of the interference function in the q_z direction. We showed that the interference along the q_z axis is a constant function for the nanoparticle monolayer. A new vertical correlation between the two layers may appear with the monolayer collapse accompanying the formation of the second nanoparticle layer as discussed in the previous section. This transition is manifested in the modulation of the X-ray scattered intensity along the truncation rod. The Fig. 7b shows the GISAXS pattern of the nanoparticle multilayer with a new peak formed along the first truncation rod (marked with dashed white line). For the nanoparticle monolayer, the intensity is at maximum at the critical exit angle, i.e. at the Yoneda peak. The formation of the second layer shifts the maximum intensity upward in the q_z direction.

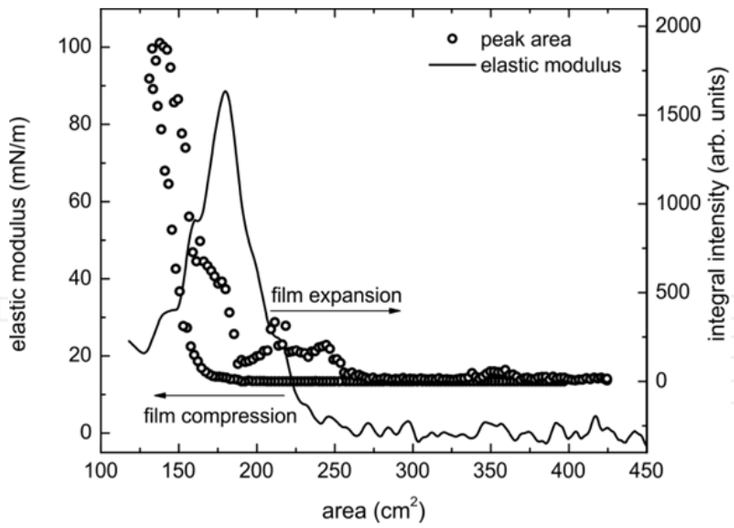

Fig. 9. The integral intensity of the first Bragg peak along the first truncation rod corresponding to the formation of a vertically correlated Ag nanoparticle multilayer as a function of the layer area.

The Fig. 9 shows the integral intensity of the newly formed Bragg peak along the first truncation rod corresponding to the vertically correlated nanoparticles as a function of the surface area. The GISAXS measurement clearly shows that the decrease in the elastic

modulus is associated with the formation of the second nanoparticle layer. Moreover we observe a hysteretic behavior during the Langmuir film decompression associated with the irreversibility of the expanded nanoparticle layer that is also documented by the interparticle distance behavior shown in Fig. 8. After opening the barriers the nanoparticle layer does not relax into a monolayer but fragments into small islands still exhibiting a certain amount of nanoparticles in the second layer (see also further). The GISAXS measurements confirmed the assumption that the fully closed nanoparticle monolayer forms short before the monolayer collapse evidenced by a maximum in surface elastic modulus.

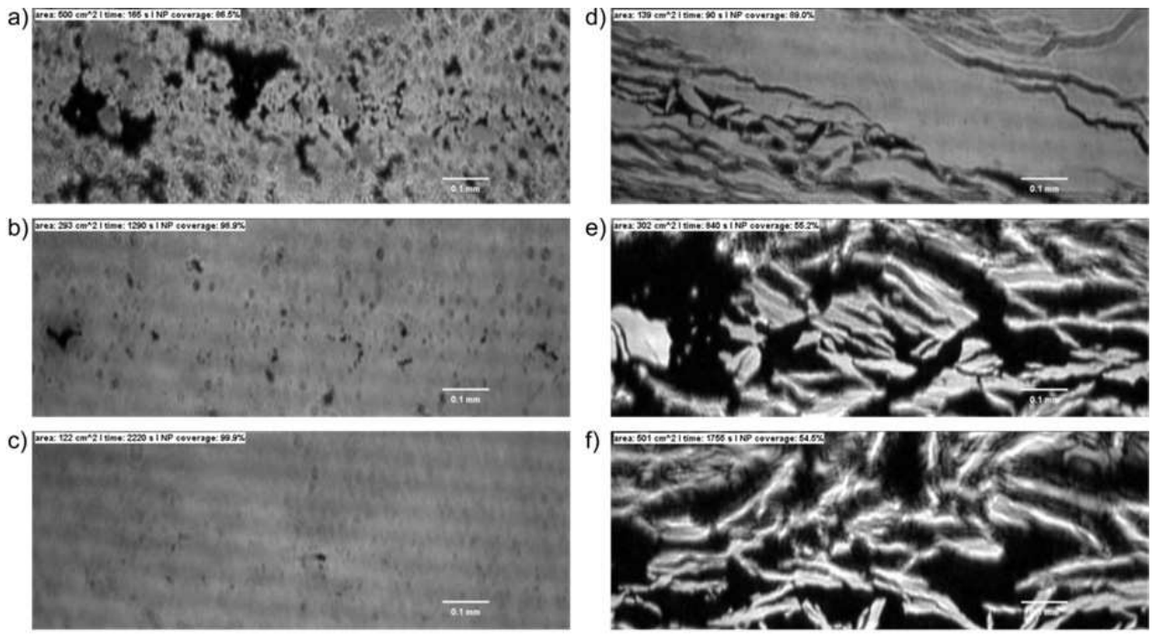

Fig. 10. The BAM images taken at surface areas a) 500 cm², b) 293 cm² and c) 122 cm² taken during the Ag nanoparticle layer compression and BAM images at surface areas d) 139 cm², e) 302 cm² and f) 501 cm² taken during the nanoparticle layer expansion.

The Brewster angle microscopy (BAM) provides further evidence of the nanoparticle monolayer formation at microscale (Henon and Meunier 1991). The laser based BAM provides much better contrast between the nanoparticle monolayer and water subphase than the conventional normal incident microscopy. The Fig. 10a)-10c) show three images taken during the nanoparticle layer compression and Fig. 10d)-10f show three images taken during the nanoparticle layer decompression. The nanoparticle layer was composed of surfactant terminated Ag nanoparticles with a core size of 6.2±0.7 nm. The nanoparticle surfactant was oleic acid. The nanoparticle layer shows vacant areas in Fig. 10a). Decreasing the film area, we close the vacancies and a compact nanoparticle monolayer forms as shown in Fig. 10c). The subsequent expansion of the nanoparticle layer is accompanied by the generation of millimeters long cracks across the nanoparticle layer as shown in Fig. 10d). A further increase of the area available for the nanoparticle expansion leads to the disruption of nanoparticle layer into micrometer large needle-like clusters as shown in Fig. 10e) and Fig. 10f). The hysteretic behavior of the nanoparticle layer at microscale during the

compression and decompression cycle is obvious and supports the interpretation of the GISAXS measurements. The Fig. 10 shows selected BAM images during the compression and expansion cycles. However we have recorded a full series of BAM images at 15 second time intervals during the compression cycle. Based on the BAM images we can calculate the average nanoparticle surface coverage based on the ratio between the bright areas that can be attributed to the nanoparticle layer and the black areas corresponding to the water subphase.

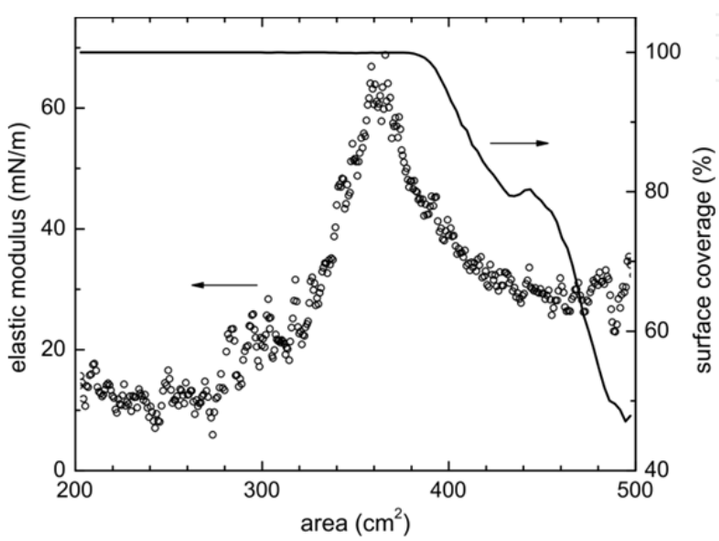

Fig. 11. The nanoparticle surface coverage based on BAM measurement along with the surface elastic modulus as a function of the Ag nanoparticle layer area during compression.

We have to keep in mind that the calculation is correct only at microscale as the nanoscale vacancies are invisible due to the BAM diffraction limit. The Fig. 11 shows the calculated nanoparticle surface coverage as a function of the film area. The graph shows also the calculated elastic modulus based on the measured nanoparticle layer surface pressure. The nanoparticle surface coverage reaches its maximum value of 100% short before the maximum in the film elastic modulus appears during the compression cycle. This is in a very good correlation with the GISAXS measurement that relates the nanoparticle monolayer collapse to the maximum in elastic modulus. The BAM measurements underestimate the nanometer-sized vacancies in the forming monolayer. This is the reason that the BAM indicate formation of nanoparticle monolayer already before the monolayer collapse. An alternative would be the imaging ellipsometry being able to track the nanoparticle layer formation at microscale more quantitatively than the BAM technique (Roth and et al. 2011).

In order to understand the formation of nanoparticle monolayer at nanoscale we deposited the nanoparticle layers on silicon substrates. The probes were deposited at different surface pressures by simply immersing the substrate into the nanoparticle covered water subphase. The selected areas of nanoparticle layers were studied by the non-contact atomic force microscopy (AFM) rather than the scanning electron microscopy as the latter one cannot provide the information on the layer height.

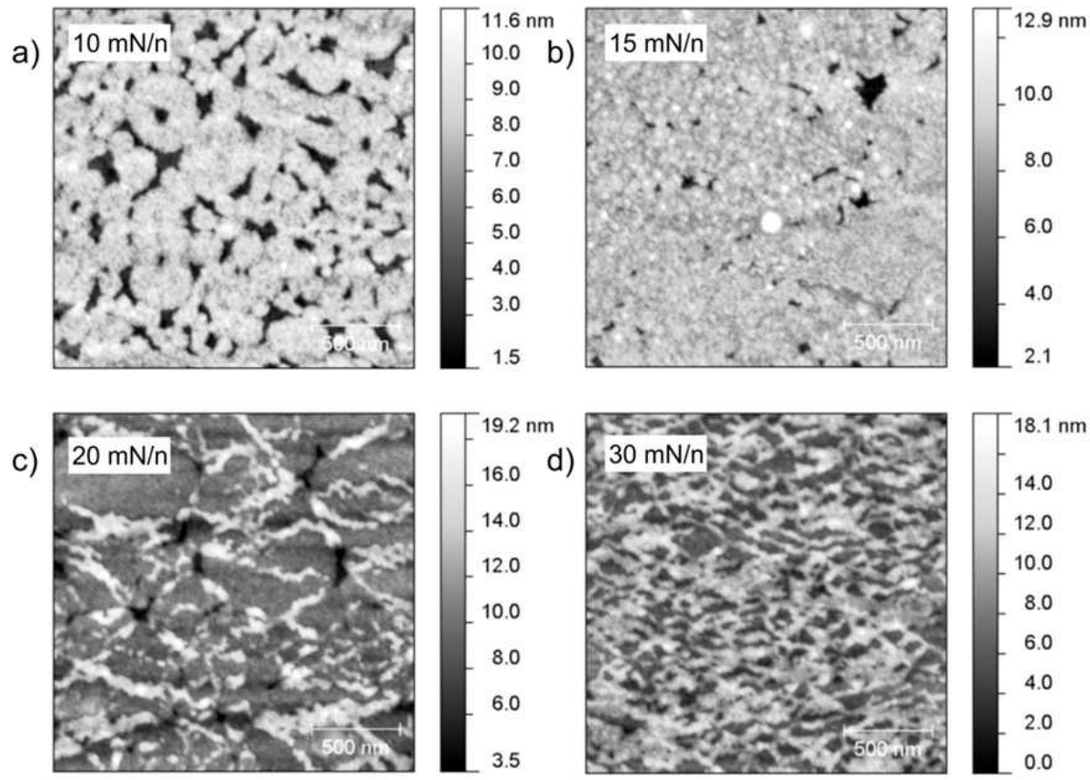

Fig. 12. The AFM images of Ag nanoparticle layers taken at the following surface pressures: a) 10 mN/m, b) 15 mN/m, c) 20 mN/m and d) 30 mN/m.

The Fig. 12 shows the AFM images of Ag nanoparticle layers deposited at different surface pressures. The nanoparticle monolayer deposited at the 10 mN/m shown in Fig. 12a displays vacancies in the nanoparticle coverage. At this stage the isolated nanoparticle clusters are coalescing into a single nanoparticle layer. The Fig. 12b shows a nanoparticle layer deposited at 15 mN/m. This AFM image shows the nanoparticle clusters forming almost a closed nanoparticle monolayer. The maximum of the surface elastic modulus was reached shortly after 15 mN/m. The AFM image shown in Fig. 12c deposited at the 20 mN/m clearly demonstrates the formation of the second nanoparticle layer after the monolayer collapse. The preferential sites for the formation of the second layer are located at the boundaries of the nanoparticle clusters. The final AFM image shown in Fig. 12d deposited at the surface pressure of 30 mN/m exhibits already a significant number of nanoparticles forming the second layer. The Fig. 13 shows calculated AFM height histograms of the nanoparticle layers deposited at different surface pressures. Only a single peak located at 6 nm corresponding to the height of monolayer is present up to the surface pressure of 15 mN/m. For the sample deposited at 20 mN/m shown in Fig. 12c, appearance of a shoulder suggests onset of formation of a second nanoparticle layer. For higher surface pressures, the newly formed peak at 12 nm in the height histogram distribution gives clear evidence of the second nanoparticle layer.

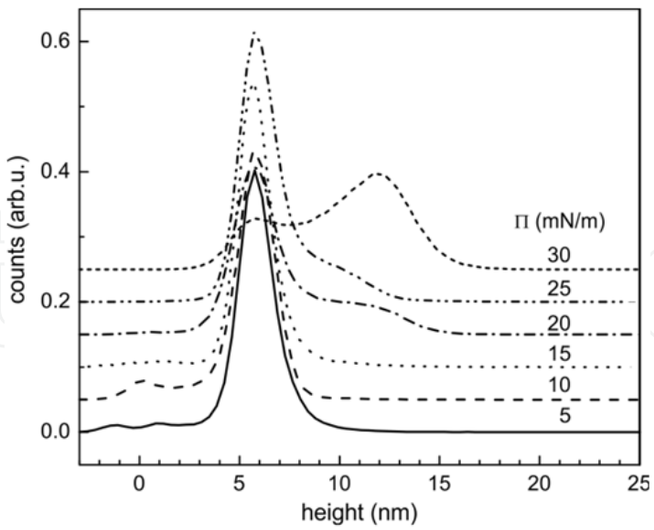

Fig. 13. The height histograms of the Ag nanoparticle layers deposited at different surface pressures obtained by analysis of the AFM images.

The number of nanoparticles occupying the second layer is steadily growing with the increasing surface pressure. At the surface pressure of 30 mN/m already more than 50% of the second nanoparticle layer was formed. The ex-situ AFM measurements provide important additional information to the in-situ GISAXS and BAM measurements. However we cannot rule out possible relaxations in the nanoparticle assemblies due to their transfer from the liquid to solid surface.

Based on the previous analyses we can conclude that the optimum deposition conditions for the nanoparticle monolayer deposition occur at the surface pressure slightly below the threshold pressure for the monolayer collapse. To achieve homogenous nanoparticle deposition over large areas of solid substrates, we modified the conventional Langmuir-Schaefer deposition (Chitu, Siffalovic et al. 2010). The scheme of the deposition trough is shown in Fig. 14.

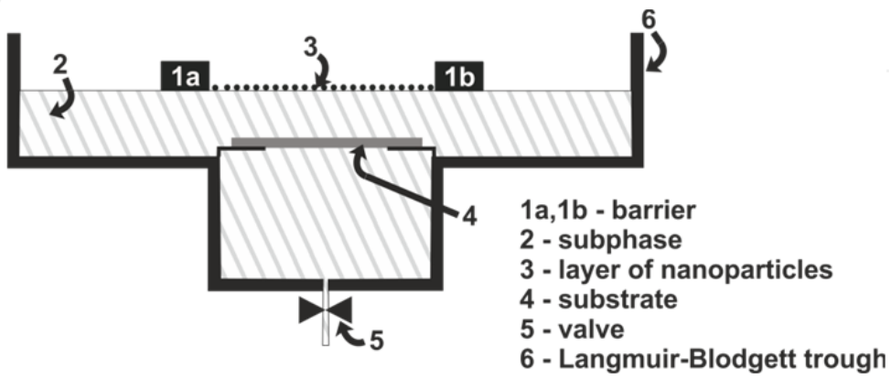

Fig. 14. The scheme of the modified Langmuir-Blodgett trough.

Differently to the conventional Langmuir-Schaefer deposition, the deposited substrate is immersed into the subphase. After spreading the nanoparticles at the water subphase and adjusting the deposition surface pressure, the water is slowly removed by opening an outlet valve. The moving water/air interface will slowly cross the inclined substrate, depositing the nanoparticle array onto it. This deposition technique produces highly homogenous nanoparticle layers on large substrates. The Fig. 15a shows a silicon wafer with the total area of some 18 cm^2 homogenously covered with an iron oxide nanoparticle monolayer (6.1±0.6 nm).

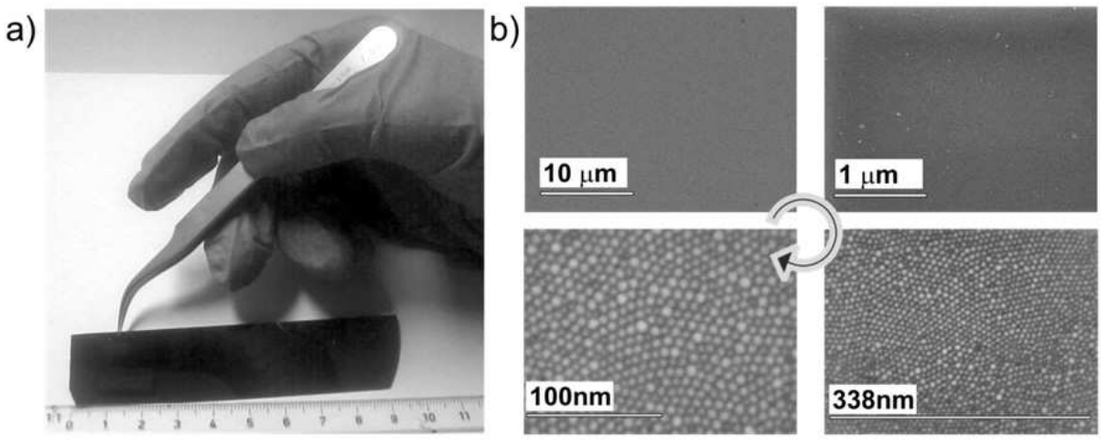

Fig. 15. a) Photograph of the homogenous Fe-O nanoparticle monolayer deposited onto silicon substrate. b) The SEM micrographs of a selected spot at the different magnifications.

To check the monolayer homogeneity we arbitrarily selected one spot at the deposited substrate and analyzed it with the SEM. The Fig. 15b shows four SEM micrographs of the selected spot at different magnification levels.

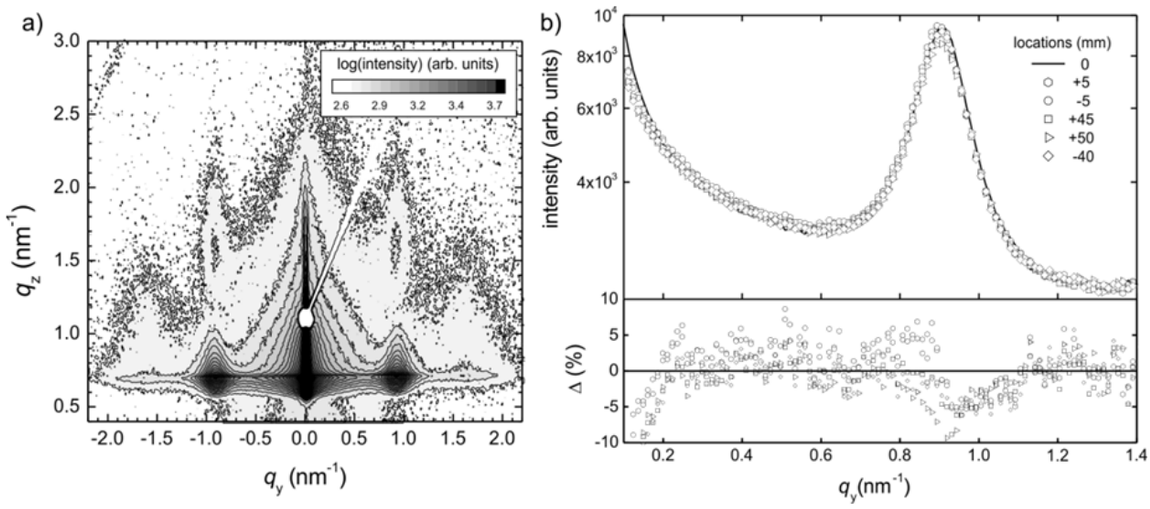

Fig. 16. a) The GISAXS pattern of the Fe-O nanoparticle monolayer. b) The extracted GISAXS line-cuts at the critical exit angle from six different locations at the substrate.

At the lowest magnification we notice the absence of any cracks in the deposited monolayer. On the contrary the traditional vertical Langmuir-Blodgett deposition is forming a series of long cracks and is not suitable for large-scale deposition. At the highest magnification we can observe a dense hexagonally ordered layer of the iron oxide nanoparticles. The SEM is suitable for detailed analysis of the selected areas of the nanoparticle monolayer but is not convenient for a rapid screening across the large areas. We have already shown that the scanning GISAXS technique provides a fast probe of the nanoparticle order at nanoscale over macroscopic areas. The Fig. 16a shows the GISAXS reciprocal space map of an arbitrarily selected location at the substrate. The integral intensity and the position of the side maxima are the measure of the nanoparticle order in the X-ray probed area. Comparing the GISAXS patterns from the different locations at the substrate we obtain the information on the homogeneity of the deposited nanoparticle monolayer. The Fig. 16b shows six line cuts extracted from the GISAXS patterns measured at different locations. The differences between the measured curves are less than ±5% that indicates a relatively high homogeneity of the deposited monolayer.

5. Processing and application of the self-assembled nanoparticle layers

In this section we focus on the issues connected with applications of deposited self-assembled nanoparticle layers. We discuss possibilities of removing the nanoparticle surfactant to increase the electrical conductivity of the nanoparticle layer as required for many applications. We address deposition of the nanoparticle layers onto thin membranes for sensor applications. We present also embedded self-assembled nanoparticle layers for organic solar cells and spintronic devices.

The surfactant molecules terminating the nanoparticles are inevitable for the synthesis and deposition of nanoparticles. However for many applications the electrical conductivity is required (Schmid 2010) while non-conductive organics is mostly used as surfactant. The surfactant molecules can be eliminated by the vacuum annealing, plasma etching, UV/ozone cleaning and many other techniques. In this section we analyze the impact of the UV/ozone cleaning on the Fe-O nanoparticle arrangement in self-assembled arrays. The UV/ozone cleaning is based on the reaction of UV light (λ=6.7 eV) with the oxygen molecules producing the highly reactive ozone. The UV light initiates photo-dissociation of the surfactant molecules that further react with the ozone molecules and are removed from the nanoparticle surface. Also a direct reaction of the surfactant molecules with the ozone molecules also called ozonolysis removes the surfactant molecules from the nanoparticle surface. In our experiment we removed the surfactant molecules from the self-assembled monolayer of iron oxide nanoparticle with the core diameter of 6.1±0.6 nm. The SEM micrographs along with the calculated nanoparticle pair correlation functions for the as-deposited sample and the sample processed in UV/ozone reactor are shown in Fig. 17a and Fig. 17b, respectively. For the as deposited nanoparticle monolayer the mean interparticle distance is given by the position of the first maximum in the pair correlation function that is 7.4 nm. After removal of the surfactant molecules terminating the nanoparticles the mean interparticle distance decreased to 6.4 nm. Moreover the nanoparticle array re-assembled into a labyrinth-like structure as shown by the SEM micrograph in Fig. 17b. This is very important for the electrical conductivity as the new nanoparticle assembly contains percolated conductive paths across the nanoparticle array.

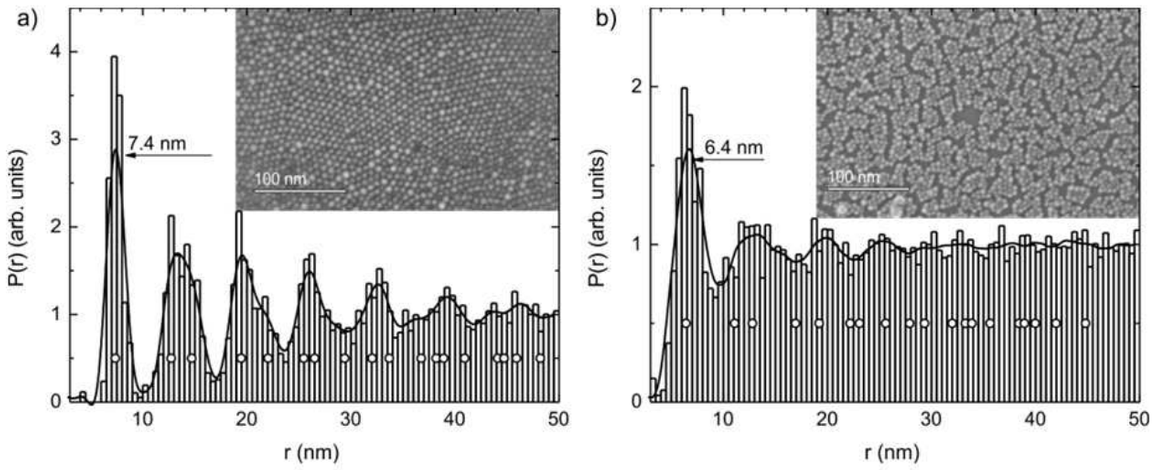

Fig. 17. The SEM micrograph and the corresponding pair correlation function for a) as deposited monolayer and b) monolayer treated in UV/ozone reactor.

We have demonstrated that the GISAXS technique is very suitable as an in-situ probe of the processes at nanoscale. We performed a time-resolved measurement of the nanoparticle re-assembly directly in the UV/ozone reactor. The above described changes in the nanoparticle pair correlation function in the direct space are manifested here as changes of the interference function in the reciprocal space. The best way of extracting the shape of the nanoparticle interference function from the GISAXS pattern is its lateral line cut along the q_y direction at the critical exit angle. The Fig. 18a shows the temporal evolution of such a line cut constructed from a series of time-resolved GISAXS frames.

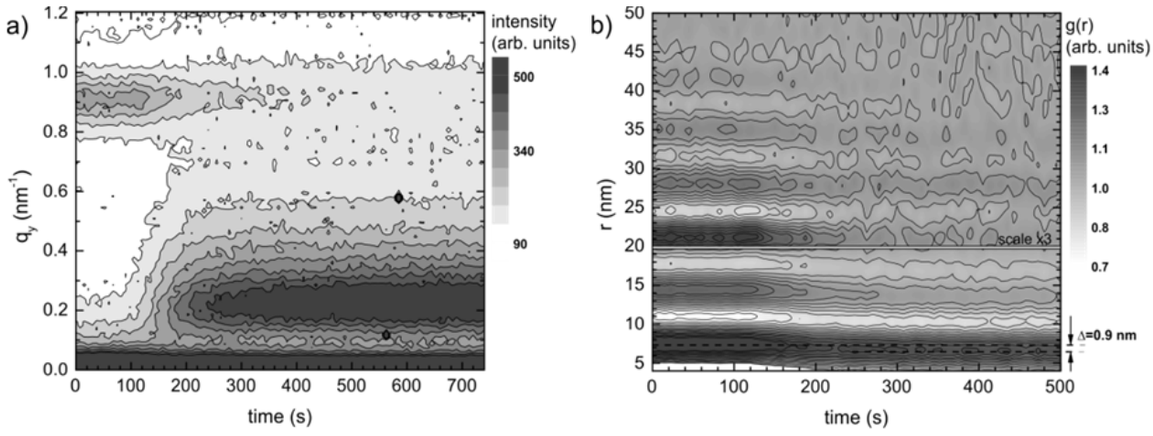

Fig. 18. a) The temporal evolution of the GISXAS line cut along the q_y direction at the critical exit angle. b) The corresponding temporal evolution of the nanoparticle pair correlation function.

The initial as-deposited self-assembled state is characterized by a maximum located at $q_y \approx 0.9nm^{-1}$. After switching on the UV/ozone reactor the maximum corresponding to the

initial self-assembled state moves slightly to higher q_y-values and its integral intensity significantly drops. Simultaneously a new peak located at $q_y \approx 0.2nm^{-1}$ develops. The new peak corresponds to the cluster formation that can be seen in the SEM micrograph in Fig. 17b. The measured GISAXS data can be recalculated into a time-resolved nanoparticle pair correlation function shown in Fig. 18b. This function reflects in detail the nanoparticle re-assembly due to the removal of the surfactant molecules. The first maximum of the pair correlation function is shifted by some 0.9 nm to lower values within the first 200 seconds. This is in full agreement with the change of the interparticle distance calculated from the SEM micrographs in Fig. 17. This example demonstrates the possibilities of GISAXS to track fast temporal changes in the nanoparticle assemblies even in the strongly reducing environments.

Application of the conductive layers composed of metal oxide nanoparticles can be exemplified on the latest generation of the Fe-O nanoparticle-based gas sensors like SO_2, NO_X, CO, O_3 and CH_4. The NO_2 sensors are of primary importance for public security as they detect trace amounts of the explosives like EGDN, TNT, PETN, RDX, etc. A large nanoparticle-covered active surface for the gas adsorption is the main advantage when compared to the conventional thin films sensors. The Fig. 19a show a complete sensor based on the metal oxide nanoparticle multilayers (Luby, Chitu et al. 2011).

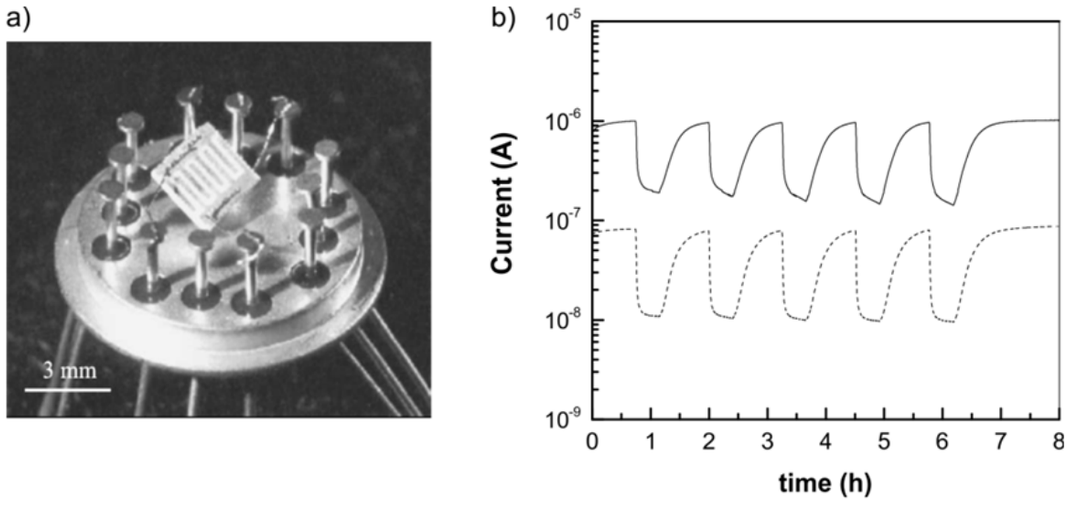

Fig. 19. a) The photograph of a nanoparticle gas sensor. b) The electrical response of the sensors fabricated with iron oxide (full line) or cobalt iron oxide (dashed line) nanoparticles.

Visible is the heating meander as the sensor working temperature is 350°C. The active area of the sensor is composed of seven monolayers of Fe_2O_3 or $CoFe_2O_4$ nanoparticles. The Fig. 19b shows the dynamic electrical response of the sensors to 5 ppm of NO_2 gas.

The nanoparticle layers exhibiting plasmonic properties in the visible and near-infrared parts of the solar spectra are potential candidates for the next generation of plasmonic solar cells (Catchpole and Polman 2008; Atwater and Polman 2010). The enhanced scattering cross-section of the plasmonic nanoparticles can efficiently trap the light into the active layer of the solar cells and to increase their external quantum efficiency.

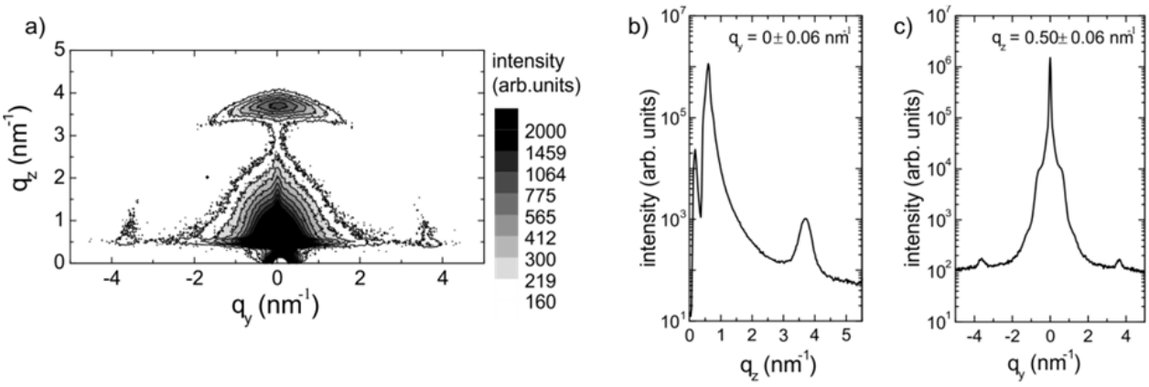

Fig. 20. a) The GISAXS reciprocal space map of the active layer deposited on Ag nanoparticle monolayer. The vertical b) and horizontal c) line-cuts across the GISAXS reciprocal space map.

The Ag nanoparticles fulfill both requirements for application in solar cells. In particular, they exhibit plasmon resonance in visible region and are highly electrically conductive. We deposited a monolayer of Ag nanoparticles (6.2±0.7 nm) at the ITO (indium tin oxide) transparent conductive layer supported on a glass substrate. Subsequently an organic active layer composed of polymer blend of P3HT (poly(3-hexylthiophene)) and PCBM (phenyl-C61-butyric acid methyl ester) of a 100 nm thickness was spin-coated on the nanoparticle monolayer. The Fig. 20a shows the GISAXS pattern of the final structure.

A prominent Bragg peak at $q_z = 3.65nm^{-1}$ originates from the molecular P3HT stacking with the inter-molecular distance of 1.7 nm and is clearly visible also in the vertical line cut in Fig. 20b The nanoparticle correlation is visible as a small peak at $q_y = 0.66nm^{-1}$ in the Fig. 20c that corresponds to the mean interparticle distance of some 9.5 nm. Here the GISAXS method provides the information on the correlations in the nanoparticle monolayer located at the buried interface hardly accessible by other analytical techniques.

Another example is the embedded nanoparticle monolayer in the hybrid tunnel junction of novel spintronic devices (Siffalovic, Majkova et al. 2009). Here the surfactant shell is inevitable to provide the tunnelling effect. The Fig. 21a shows schematically the multilayer structure containing iron oxide nanoparticle monolayer. The first fabrication step is the vacuum deposition of a metallic layer forming the bottom electrode. The second step is the deposition of the nanoparticle monolayer that is overcoated by another vacuum deposited metallic layer in the final step. The Fig. 21b shows the evolution of a line cut in the GISAXS pattern with the growing thickness of the metallic overlayer. The peak at $q_y = 0.83nm^{-1}$ marked with the dashed line corresponding to the nanoparticle layer can be seen throughout the entire deposition process. These examples demonstrate that the buried nanoparticle monolayer confined to the interface with a thin metallic film can be monitored using the GISAXS technique.

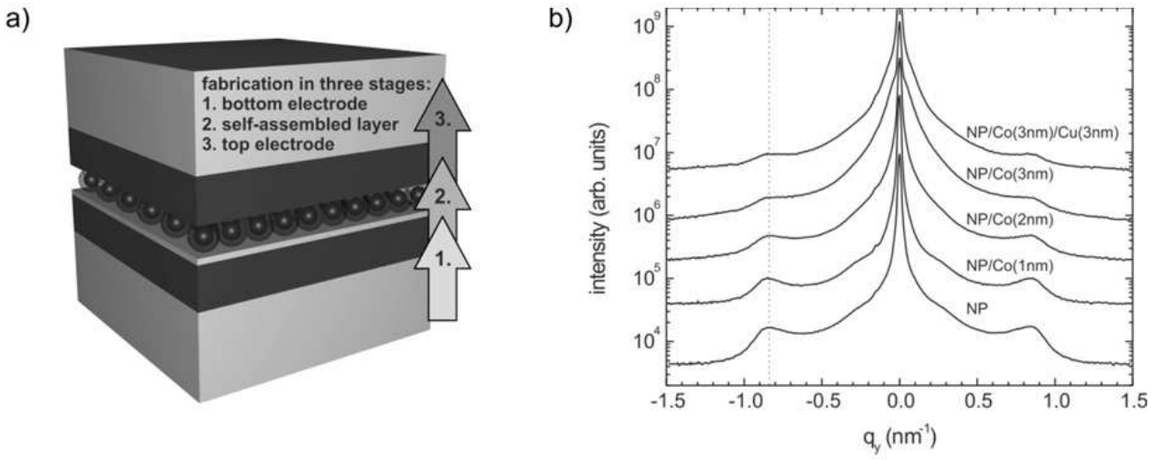

Fig. 21. a) A sketch of the spintronic structure that contains a Fe-O nanoparticle monolayer. b) Extracted line-cuts from the GISAXS reciprocal space maps at the critical exit angle in the different fabrication stages of spintronic structure.

The nanoparticle monolayers and multilayers can be deposited also on flexible membranes to be employed for monitoring mechanical properties like strain (Herrmann, Müller et al. 2007). The principle of a strain sensor is based on a change of electrical current across the nanoparticle layer as a function of the applied mechanical stress that modifies the interparticle distance in the film and consequently the electrical resistivity. The sensitivity of the nanoparticle-based strain sensors is roughly by two orders of magnitude better than that of the conventional thin metallic film ones. We investigated the nanoscale response of the nanoparticle monolayer to the applied external stress (Siffalovic, Chitu et al. 2010). We deposited a monolayer composed of iron oxide nanoparticles (6.2±0.7 nm) onto a mylar foil (1 μm thickness). The mylar foil was fixed in a stretching device for in-situ SAXS tensile stress measurements as shown in Fig. 22a.

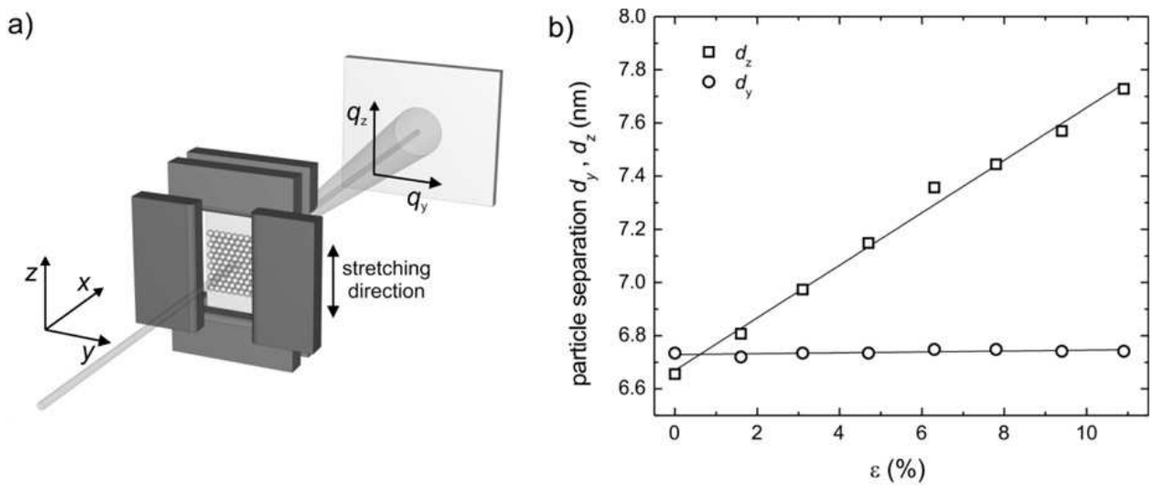

Fig. 22. a) Scheme of the experimental setup with an in-situ SAXS tensile stage. b) The evaluated interparticle separation as a function of the strain in two perpendicular directions.

The mylar foil was strained up to 11% in the *z*-direction and the SAXS patterns were recorded. Relying on them, the mean interparticle distance was evaluated in the applied stress direction and in the direction perpendicular to it. The results are shown in Fig. 22b. In the direction perpendicular to the applied stress the nanoparticle separation remained constant. However in the direction of the applied stress the interparticle distance followed linearly the measured foil strain. These measurements provide the test basis for the future strain sensors based on the nanoparticle layers.

In this section we included only a few of a large variety of practical applications of the nanoparticle monolayers. The nanoparticle deposition, eventual post-deposition processing of the nanoparticle layer and the test measurements of the macroscopic properties of interest are common for all these applications. The presented SAXS/GISAXS techniques offer an efficient and direct access to the nanoparticle arrangement within the final device.

6. Conclusion

The chapter provides an introductory guide to X-ray scattering studies of nanoparticle self-assembly processes at liquid/air and solid/air interfaces. It is primarily intended for graduate and post-graduate students but it is aimed also at other scientific community in the field addressing the issues of general interest. In particular, it shows the latest advances in the rapidly growing field of self-assembled nanoparticle layers. The X-ray scattering diagnostic technique was reviewed that provides an easy access even to buried nanoparticle assemblies. The main advantage of the X-ray scattering analysis is the possibility to track technologically important processes connected with the nanoparticle self-assembly or re-assembly in real time. The self-assembly process after colloidal drop casting and

evaporation was described shortly while a detailed study of the self-assembly process at the liquid/air interface was the core of the chapter. This interface represents an ideal system for the nanoparticle assembling as the nanoparticles are confined to the interface but still keep translational mobility along it. The processes accompanying the formation of a nanoparticle monolayer and its transition to a multilayer were described in detail. Ideal deposition conditions for the nanoparticle monolayer formation were derived relying on the surface pressure and surface elastic modulus measurements. A modified Langmuir-Schaefer technique suitable for large-area deposition of nanoparticle arrays was presented. Selected applications of the deposited self-assembled layers were reviewed.

It has to be stressed that the colloidal nanoparticle self-assembly is a complex process resulting from an interplay between many factors where the nanoparticle type and size as well as the chemical composition of surfactant play a crucial role. Therefore none of the self-assembly techniques described in the chapter is generally applicable to any colloidal nanoparticle solution. It is also the reason why different techniques were presented with different types of nanoparticles.

It has to be also noted that in addition to the spontaneous nanoparticle self-assembly treated in this chapter of limited length, other approaches to assembling based on recent developments are of growing interest in the nanoparticle community. These include e.g. directed self-assembly of nanoparticles on pre-patterned substrates, chemically driven self-assembly, nanoparticle self-assembly stimulated by a magnetic or electro-magnetic field.

7. Acknowledgment

This publication is the result of the project implementation Center of Applied Nanoparticle research, ITMS code 26240220011, supported by the Research & Development Operational Program funded by the ERDF. The support of Grant Agency VEGA Bratislava, project No. 2/0041/11, is also acknowledged.

8. References

Atwater, H. A. and Polman, A. (2010). Plasmonics for improved photovoltaic devices. *Nature Materials* 9(3): 205-213.

Barnes, G., Gentle, I., et al. (2005). *Interfacial science: an introduction*. Oxford [u.a.], Oxford Univ. Press.

Born, M. and Wolf, E. (1999). *Principles of optics: electromagnetic theory of propagation, interference and diffraction of light*. Cambridge; New York, Cambridge University Press.

Catchpole, K. R. and Polman, A. (2008). Design principles for particle plasmon enhanced solar cells. *Applied Physics Letters* 93(19): 191113.

Chitu, L., Siffalovic, P., et al. (2010). Modified Langmuir-Blodgett deposition of nanoparticles - measurement of 2D to 3D ordered arrays. *Measurement Science Review* 10(5): 162-165.

Chushkin, Y., Ulmeanu, M., et al. (2003). Structural study of self-assembled Co nanoparticles. *Journal of Applied Physics* 94(12): 7743-7748.

Daillant, J. and Gibaud, A. (2009). *X-ray and neutron reflectivity : principles and applications*. Berlin Heidelberg, Springer.

Deegan, R. D., Bakajin, O., et al. (1997). Capillary flow as the cause of ring stains from dried liquid drops. *Nature* 389(6653): 827-829.

Feigin, L. A., Svergun, D. I., et al. (1987). *Structure analysis by small-angle X-ray and neutron scattering*. New York [etc.], Plenum Press.

Feldheim, D. L. (2002). *Metal nanoparticles: synthesis, characterization, and applications*. New York [u.a.], Dekker.

Glatter, O. and Kratky, O. (1982). *Small angle x-ray scattering*. London; New York, Academic Press.

Guinier, A. (1963). *X-ray diffraction in crystals, imperfect crystals, and amorphous bodies*. San Francisco,, W.H. Freeman.

Guinier, A. and Fournet, G. (1955). *Small-angle scattering of X-rays*. New York,, Wiley.

Henon, S. and Meunier, J. (1991). Microscope at the Brewster-Angle - Direct Observation of 1st-Order Phase-Transitions in Monolayers. *Review of Scientific Instruments* 62(4): 936-939.

Herrmann, J., Müller, K. H., et al. (2007). Nanoparticle films as sensitive strain gauges. *Applied Physics Letters* 91(18): 183105.

Holý, V., Pietsch, U., et al. (1999). *High-resolution X-ray scattering from thin films and multilayers*. Berlin; New York, Springer.

Hosemann, R. and Bagchi, S. N. (1962). *Direct analysis of diffraction by matter*. Amsterdam, North-Holland Publ. Comp.

Kittel, C. (2005). *Introduction to solid state physics*. Hoboken, NJ, Wiley.

Kraft, P., Bergamaschi, A., et al. (2009). Performance of single-photon-counting PILATUS detector modules. *Journal of Synchrotron Radiation* 16(3): 368-375.

Lazzari, R. (2002). IsGISAXS: a program for grazing-incidence small-angle X-ray scattering analysis of supported islands. *Journal of Applied Crystallography* 35: 406-421.

Lazzari, R. (2009). Grazing Incidence Small-Angle X-Ray Scattering from Nanostructures. In: *X-ray and Neutron Reflectivity*. J. Daillant and A. Gibaud, Springer Berlin / Heidelberg. 770: 283-342.

Luby, S., Chitu, L., et al. (2011). Oxide nanoparticle arrays for sensors of CO and NO2 gases. *Vacuum* In Press, Corrected Proof.

Michaelsen, C., Wiesmann, J., et al. (2002). Recent developments of multilayer mirror optics for laboratory x-ray instrumentation. *X-Ray Mirrors, Crystals, and Multilayers Ii* 4782: 143-151.

Müller-Buschbaum, P. (2009). A Basic Introduction to Grazing Incidence Small-Angle X-Ray Scattering. In: *Applications of Synchrotron Light to Scattering and Diffraction in Materials and Life Sciences*. M. Gomez, A. Nogales, M. C. Garcia-Gutierrez and T. A. Ezquerra, Springer Berlin / Heidelberg. 776: 61-89.

Nagarajan, R. (2008). *Nanoparticles: synthesis, stabilization, passivation, and functionalization*. Washington, DC, American Chemical Soc.

Niederberger, M. and Pinna, N. (2009). Metal Oxide Nanoparticles in Organic Solvents Synthesis, Formation, Assembly and Application. *Engineering Materials and Processes*. London, Springer London.

Park, J., An, K., et al. (2004). Ultra-large-scale syntheses of monodisperse nanocrystals. *Nature Materials* 3(12): 891-895.

Pileni, M.-P. (2005). *Nanocrystals forming mesoscopic structures*. Weinheim, Wiley-VCH.

Renaud, G., Lazzari, R., et al. (2009). Probing surface and interface morphology with Grazing Incidence Small Angle X-Ray Scattering. *Surface Science Reports* 64(8): 255-380.

Roth, S. V., Dohrmann, R., et al. (2006). Small-angle options of the upgraded ultrasmall-angle x-ray scattering beamline BW4 at HASYLAB. *Review of Scientific Instruments* 77(8): 085106.

Roth, S. V. and et al. (2011). In situ observation of cluster formation during nanoparticle solution casting on a colloidal film. *Journal of Physics: Condensed Matter* 23(25): 254208.

Rycenga, M., Cobley, C. M., et al. (2011). Controlling the Synthesis and Assembly of Silver Nanostructures for Plasmonic Applications. *Chemical Reviews* 111(6): 3669-3712.

Salditt, T., Metzger, T. H., et al. (1994). Kinetic Roughness of Amorphous Multilayers Studied by Diffuse-X-Ray Scattering. *Physical Review Letters* 73(16): 2228-2231.

Schmid, G. (2010). *Nanoparticles from theory to application*. Weinheim, Wiley-VCH.

Siffalovic, P., Chitu, L., et al. (2010). Kinetics of Nanoparticle Reassembly Mediated by UV-Photolysis of Surfactant. *Langmuir* 26(8): 5451-5455.

Siffalovic, P., Chitu, L., et al. (2010). Towards strain gauges based on a self-assembled nanoparticle monolayer-SAXS study. *Nanotechnology* 21(38).

Siffalovic, P., Jergel, M., et al. (2011). GISAXS - probe of buried interfaces in multilayered thin films. In: *X-Ray Scattering*. C. M. Bauwens. New York, Nova Science Publishers.

Siffalovic, P., Majkova, E., et al. (2009). Fabrication and Characterization of Hybrid Tunnel Magnetoresistance Structures with Embedded Self-Assembled Nanoparticle Templates. *Acta Physica Polonica a* 115(1): 332-335.

Siffalovic, P., Majkova, E., et al. (2008). Real-Time Tracking of Superparamagnetic Nanoparticle Self-Assembly. *Small* 4(12): 2222-2228.

Siffalovic, P., Majkova, E., et al. (2007). Self-assembly of iron oxide nanoparticles studied by time-resolved grazing-incidence small-angle x-ray scattering. *Physical Review B* 76(19).

Siffalovic, P., Vegso, K., et al. (2010). Measurement of nanopatterned surfaces by real and reciprocal space techniques. *Measurement Science Review* 10(5): 153-156.

Stribeck, N. (2007). *X-ray scattering of soft matter*. Berlin, Springer.

Ulman, A. (1991). *An introduction to ultrathin organic films : from Langmuir-Blodgett to self-assembly*. Boston [u.a.], Acad. Press.

Vegso, K., Siffalovic, P., et al. (2011). In situ GISAXS monitoring of Langmuir nanoparticle multilayer degradation processes induced by UV photolysis. *physica status solidi (a)*: (accepted, in press).

Wiesmann, J., Graf, J., et al. (2009). X-Ray Diffractometry with Low Power Microfocus Sources - New Possibilities in the Lab. *Particle & Particle Systems Characterization* 26(3): 112-116.

Yoneda, Y. (1963). Anomalous Surface Reflection of X Rays. *Physical Review* 131(5): 2010.

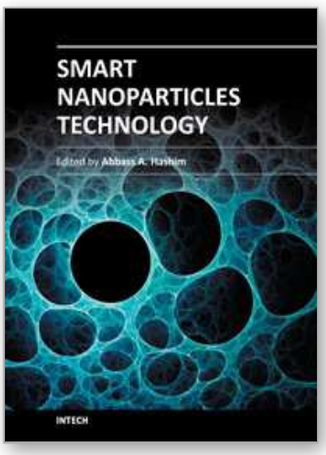

Smart Nanoparticles Technology

Edited by Dr. Abbass Hashim

ISBN 978-953-51-0500-8
Hard cover, 576 pages
Publisher InTech
Published online 18, April, 2012
Published in print edition April, 2012

In the last few years, Nanoparticles and their applications dramatically diverted science in the direction of brand new philosophy. The properties of many conventional materials changed when formed from nanoparticles. Nanoparticles have a greater surface area per weight than larger particles which causes them to be more reactive and effective than other molecules. In this book, we (InTech publisher, editor and authors) have invested a lot of effort to include 25 most advanced technology chapters. The book is organised into three well-heeled parts. We would like to invite all Nanotechnology scientists to read and share the knowledge and contents of this book.

How to reference

In order to correctly reference this scholarly work, feel free to copy and paste the following:

Peter Siffalovic, Eva Majkova, Matej Jergel, Karol Vegso, Martin Weis and Stefan Luby (2012). Self-Assembly of Nanoparticles at Solid and Liquid Surfaces, Smart Nanoparticles Technology, Dr. Abbass Hashim (Ed.), ISBN: 978-953-51-0500-8, InTech, Available from: http://www.intechopen.com/books/smart-nanoparticles-technology/self-assembly-of-nanoparticles-at-solid-and-liquid-surfaces

INTECH
open science | open minds

InTech Europe
University Campus STeP Ri
Slavka Krautzeka 83/A
51000 Rijeka, Croatia
Phone: +385 (51) 770 447
Fax: +385 (51) 686 166
www.intechopen.com

InTech China
Unit 405, Office Block, Hotel Equatorial Shanghai
No.65, Yan An Road (West), Shanghai, 200040, China
中国上海市延安西路65号上海国际贵都大饭店办公楼405单元
Phone: +86-21-62489820
Fax: +86-21-62489821

IntechOpen